Droop Controlled Microgrid With Intelligent PV-DSTATCOM for Power Quality Improvement

Faa-Jeng Lin, *Fellow, IEEE*, Kuang-Hsiung Tan, *Member, IEEE*, Zhao-Yun Kuan, and Chen-Yi Wang

***Abstract*—A droop controlled microgrid composed of a battery energy storage system and a photovoltaic-based distribution static compensator (PV-DSTATCOM) is developed in this article to improve the power quality of a microgrid. Owing to the high penetration rate of the renewable energy source-based distributed generators, the extensive usage of inductive loads and unexpected load change, the power quality issues, including unbalanced currents, current harmonics, and lagging power factor (PF), have become severe challenges in the microgrid. Consequently, a novel control scheme of PV-DSTATCOM is developed to overcome the power quality issues in the droop controlled microgrid. The developed PV-DSTATCOM combines the power generated from PV system with the reactive power compensation of a DSTATCOM to enhance power quality and grid reliability. In other words, the developed PV-DSTATCOM owns the angular frequency/active power $\omega-P$ droop characteristic and the ability to reduce the total harmonic distortion of the current, correct PF, compensate the reactive power for voltage support, and mitigate the three-phase unbalanced system currents of the microgrid. Furthermore, to effectively improve the transient response of the reactive power compensation and the performance of the PV-DSTATCOM during load variations, an intelligent online trained Petri Legendre fuzzy neural network (PLFNN) controller is proposed to replace the conventional proportional-integral controller. Furthermore, the network structure and the online learning algorithm of the proposed PLFNN are derived in detail. Finally, the effectiveness of the proposed PLFNN-based PV-DSTATCOM to improve the power quality of the microgrid is verified by the experimentation.**

***Index Terms*—Battery energy storage system (BESS), intelligent control, Legendre fuzzy neural network (PLFNN), microgrid, photovoltaic-based distribution static compensator (PV-DSTATCOM), total harmonic distortion (THD).**

NOMENCLATURE

v_{sa}, v_{sb}, v_{sc}	Three-phase voltages of BESS.
ω_s	Actual angular frequency of microgrid.
θ_s	Electric angle.
i_{sa}, i_{sb}, i_{sc}	Three-phase currents of BESS.
V_{sd}, V_{sq}	*dq*-axis voltages of BESS.
I_{sd}, I_{sq}	*dq*-axis currents of BESS.
$V_{an,peak}$	Peak value of phase voltage of microgrid.
P_s	Active power output of BESS.
Q_s	Reactive power output of BESS.
ω_m^*	Angular frequency command of BESS.
V_m^*	Amplitude command of phase voltage.
ω_n	Reference angular frequency of BESS at no load.
V_n	Reference amplitude of phase voltage.
K_{sp}	Droop coefficient of $P-\omega$ droop characteristic in BESS.
K_{sq}	Droop coefficient of *Q-V* droop characteristic in BESS.
P_n	Reference active power.
Q_n	Reference reactive power.
θ_m^*	Electric angle for coordinate transformation.
I_{sd}^*, I_{sq}^*	*dq*-axis current commands of BESS.
u_{coma}, u_{comb}, u_{comc}	Three-phase reference commands of BESS.
v_{pa}, v_{pb}, v_{pc}	Three-phase voltages of PV-DSTATCOM.
i_{pa}, i_{pb}, i_{pc}	Three-phase currents of PV-DSTATCOM.
P_p	Active power output of PV-DSTATCOM.
i_{La}, i_{Lb}, i_{Lc}	Three-phase load currents.
I_{Ld}, I_{Lq}	*dq*-axis load currents.
$\tilde{I}_{Ld}, \tilde{I}_{Lq}$	*dq*-axis ac current components of load.
$\bar{I}_{Ld}, \bar{I}_{Lq}$	*dq*-axis dc current components of load.
I_{Qd}^*	*d*-axis reactive power command.
P_{pref}	Reference active power.
P_{pm}^*	Active power command.
$K_{p\omega}$	Droop coefficient of $\omega-P$ droop characteristic in PV-DSTATCOM.
ω_{pn}	Reference angular frequency.
I_{pd}^*, I_{pq}^*	*dq*-axis current commands of PV-DSTATCOM.
u_u, u_v, u_w	Three-phase reference commands of PV-DSTATCOM.
x_i^1	Inputs of PLFNN.
σ_{im}^2	Standard deviation of Gaussian function.
m_{im}^2	Mean of Gaussian function.

Received 15 October 2024; revised 8 March 2025; accepted 14 May 2025. Date of publication 20 May 2025; date of current version 30 June 2025. This work was supported by the National Science and Technology Council of Taiwan, R.O.C. under Grant NSTC 113-2218-E-008-016. Recommended for publication by Associate Editor M. Tavakoli Bina. *(Corresponding author: Faa-Jeng Lin.)*

Faa-Jeng Lin, Zhao-Yun Kuan, and Chen-Yi Wang are with the Department of Electrical Engineering, National Central University, Chungli 320317, Taiwan (e-mail: linfj@ee.ncu.edu.tw; 111521098@cc.ncu.edu.tw; 112521137@cc.ncu.edu.tw).

Kuang-Hsiung Tan is with the Department of Electrical and Electronic Engineering, Chung Cheng Institute of Technology, National Defense University, Taoyuan 334301, Taiwan (e-mail: tankh@ccit.ndu.edu.tw).

Color versions of one or more figures in this article are available at https://doi.org/10.1109/TPEL.2025.3571917.

Digital Object Identifier 10.1109/TPEL.2025.3571917

y_{im}^2	Outputs of membership layer.
λ_l^3	Output of Legendre expansion.
λ	Vector output of Legendre expansion.
L_h	Legendre polynomials.
y_l^3	lth node output of Legendre layer.
w_l^3	Connected weights of Legendre layer.
t_{ip}^4	Transition of Petri layer.
d_{ip}	Dynamic threshold value.
α, β	Positive constants.
y_{ip}^4	Output of Petri layer.
y_r^5	rth node output of rule layer.
w_r^6	Connective weight between the output layer and rule layer.
y_o^6	Output of proposed PLFNN controller.
E	Energy function.
Δw_r^6	Update of connected weight.
η_r	Learning rate.
Δw_l^3	Update of connected weight.
η_l	Learning rate.
$\Delta \sigma_{im}^2$	Update of standard deviation.
Δm_{im}^2	Update of mean.
η_σ	Learning rate.
η_m	Learning rate.

I. Introduction

In THE past decades, a novel conceptual small-scale power system denominated microgrid had been proposed to integrate the renewable energy resource-based distributed generators (DGs), such as photovoltaic (PV) system, wind turbine generator, and battery energy storage system (BESS), into the local power distribution systems due to the increasing concerns regarding the energy crisis, greenhouse gas emission reduction and environmental protection [1], [2], [3]. The microgrid possesses the capability of operating in islanded mode or grid-connected mode to enhance the power supply reliability [4], [5]. Moreover, in the light of control strategy, the droop control method is a popular control algorithm for the microgrid owing to the merits, such as high flexibility and reliability [6], [7]. The droop control method is to regulate the system voltage and frequency to share the reactive and active powers among the DGs in accordance with the power demand of the loads without communication requirement [7], [8]. Hence, the characteristics of the droop control method are similar to the synchronous generators [2]. Nevertheless, on account of the stochastic and intermittent characteristics of the renewable energy resources, the power quality of the microgrid gets severe challenges compared with the traditional power system [9], [10]. Furthermore, with the extensive usage of the inductive, nonlinear, and unbalanced loads at the customer's side, the lagging power factor (PF), harmonic pollution, and unbalanced system currents also deteriorate the power quality and grid reliability [11], [12], [13]. In other words, the inordinate reactive power demand from the inductive load reduces the active power transfer capability and increases the feeder losses. The nonlinear load in power system also causes low operating efficiency. In addition, the safe operation of the generators and transformers will be threatened by the unbalanced currents [11], [12]. Accordingly, how to solve the power quality problems resulted from the renewable energy resources and the dirty loads in the droop controlled microgrid is a significant issue.

The distributed static compensator (DSTATCOM) is an effective method to overcome the power quality problems and is widely adopted to mitigate the current-based power quality problems [13], [14], [15]. The main purpose of the DSTATCOM is to inject the controlled currents of particular magnitudes and phase angles into the grid for the grid current to be sinusoidal and in phase with the grid voltage [16]. Moreover, the common control algorithms of the DSTATCOM are the instantaneous reactive power (IRP) theory and the synchronous reference frame (SRF) method [10], [17]. The principle of the IRP theory is to compute the instantaneous active and reactive powers of the loads to achieve the objective of the power quality improvement [10]. Though the IRP is easy to implement in the DSTATCOM due to the operation in $\alpha\beta$ stationary reference frame without using the phase-locked loop (PLL), the accurate calculation of the instantaneous power is difficult to achieve in the three-phase unbalanced system [18]. On the other hand, the SRF method is mainly implemented in dq synchronously rotating reference frame to dispatch the controlled currents for solving the power quality problems. Because the control accuracy of the dq synchronously rotating reference frame-based technique is higher than the $\alpha\beta$ stationary reference frame-based technique, the SRF method is more suitable than the IRP theory for the DSTATCOM [19].

The conventional proportional-integral (PI) controller has been generally adopted in consequence of the simple structure and easy implementation. However, because the designed and fixed gains of the PI controller are only suitable for the assumed scenarios, the performance of the control system using PI controller will be decreased on account of the external disturbance and interference such as sudden load change and short-circuit faults [2], [10], [20]. Moreover, the PI controller cannott provide favorable control performance if the controlled plant has nonlinear and uncertain factors such as the existence of a nonlinear load [21]. Hence, though the PI-based DSTATCOM can reduce the total harmonic distortion (THD) of the current, the poor control efficacy and sluggish dynamics of the DSTATCOM during the fast load change are resulted from the poor disturbance rejection property of the adopted PI controller [13], [15], [22]. Furthermore, though the model-based nonlinear controller has been provided in the literature and the parameters can be optimized under the assumed ideal conditions, it cannot effectively deal with the external disturbance and interference resulted in poor system stability and control performance [21], [23]. In addition, the structure of the model-based controller is complicated in nature and requires exact model of the process, which leads to a discrepancy in the actual and mathematical models [23], [24]. Therefore, how to design the suitable controller for coping with the inevitable nonlinear and uncertain factors in the power system is a significant issue.

In the past decades, the Petri fuzzy neural network (PFNN) has been developed and applied in different fields [25]. The PFNN

mainly comprises the Petri net (PN) and fuzzy neural network (FNN). The PN is an effective algorithm to analyze and model the discrete event system with synchronization, concurrence, sequencing, and sharing of resources [26]. Moreover, the PN can effectively implement the real-time and desynchronized control with the superior analysis and graphical function [27], [28]. Thus, the PFNN owns the capabilities of PN to analyze, model, optimize, and control the dynamic system, the abilities of fuzzy logic algorithm to cope with uncertain information and the capabilities of neural network (NN) in learning, approximation, generalization, and parallel computation. Therefore, much literature using the PFNN has been proposed in [28] and [29]. In [28], a storage system using the PFNN was proposed for the voltage stabilization control in a microgrid system. The PFNN controlled squirrel-cage induction generator was developed in [29] for the grid-connected wind power applications. Additionally, the Legendre polynomials are a set of completely orthogonal polynomials and can approximate any function to arbitrary precision within a bounded interval [30], [31]. In other words, the Legendre polynomials can expand the original input vector with faster convergence rate and lower computational burden, and generate nonlinear transformations [32]. Some researches using the Legendre polynomials for different applications have been provided [32], [33]. In [33], the Legendre polynomials were adopted for a permanent-magnet assisted synchronous reluctance motor drive system to achieve the accurate control performance in terms of speed tracking control. Consequently, on account of the merits of the PFNN and the Legendre polynomials, a novel intelligent controller to integrate the Legendre polynomials into the PFNN denominated as Petri Legendre fuzzy neural network (PLFNN) is firstly proposed in this article.

In this article, a droop controlled microgrid composed of a BESS and a PV system is built. To efficiently utilize the capabilities of renewable energy, a PV-based DSTATCOM (PV-DSTATCOM) with a novel control scheme is developed, combining the power generation from PV system with the reactive power compensation of a DSTATCOM to enhance power quality and grid reliability. Additionally, the developed PV-DSTATCOM owns the angular frequency/active power $\omega-P$ droop characteristic and the ability of the DSTATCOM for the power quality improvement and voltage support. Moreover, to solve the poor control property of the conventional PI controller, a PLFNN is proposed for the PV-DSTATCOM to replace the PI controller. The rest of this article is organized given as follows: The theories of the droop controlled microgrid and the novel control scheme of the PV-DSTATCOM are particularized in Section II. Then, the network structure of the proposed PLFNN controller for the developed PV-DSTATCOM is derived in Section III. Furthermore, in Section IV, the effectiveness of the proposed PLFNN-based PV-DSTATCOM in the microgrid to reduce the current THD, correct PF, compensate the reactive power for voltage support, and mitigate the three-phase unbalaced system currents is verified by the experimentation. The experimental results of various other controllers including PI and non-model-based neural network controllers are also provided for the comparison of control performance. Finally, Section V concludes this article.

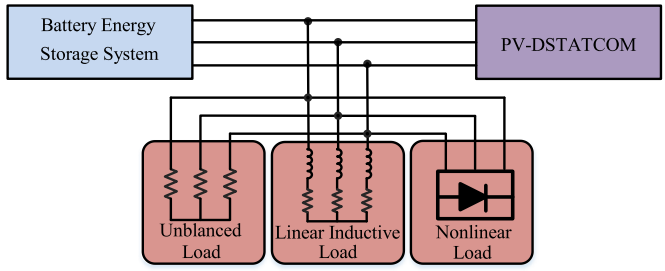

Fig. 1. Schematic framework of droop controlled microgrid.

II. Droop Controlled Microgrid With PV-DSTATCOM

The schematic framework of the droop controlled microgrid is given in Fig. 1. The BESS and PV-DSTATCOM are connected in parallel through the power inverters. The loads consist of the nonlinear load, unbalanced load and linear inductive load to generate the deteriorated current harmonics, unbalanced system currents, and lagging PF. The system frequency and voltage of the developed microgrid are 60 Hz and 110 *V*rms, respectively. Then, the detailed control schemes of the BESS and the PV-DSTATCOM for the power quality improvement are described in the following.

A. Control Scheme of BESS

The schematic diagram of the BESS is provided in Fig. 2. The control block of the BESS with droop control is illustrated in Fig. 2(a). The active power/angular frequency $P-\omega$ and reactive power/voltage Q–V droop characteristics of the BESS are presented in Fig. 2(b) and (c), respectively. In this article, a second-order generalized integrator phase locked loop (SOGI-PLL) is adopted in the BESS to exactly synchronize with the system voltage of the microgrid [34]. On the whole, the conventional PLL fails to accurately synchronize with the voltage during unbalanced voltage situation in consequence of the presence of the double-frequency ac components and dc components in dq frame [34], [35]. Therefore, the SOGI-PLL is widely adopted to replace the conventional PLL and the objective is to extract the positive sequence components of the system voltage to solve the inaccurate synchronization during unbalanced voltage situation [35], [36]. In accordance with the SOGI-PLL, the electric angle θ_s and actual angular frequency ω_s of the microgrid are obtained. Furthermore, to implement the droop control for the BESS, the three-phase voltages v_{sa}, v_{sb}, v_{sc} and three-phase currents i_{sa}, i_{sb}, i_{sc} of the BESS are utilized to compute the dq-axis voltages V_{sd}, V_{sq} and currents I_{sd}, I_{sq} according to the abc/dq coordinate transformation as shown in Fig. 2(a). Hence, the peak value of the phase voltage $V_{an,peak}$ of the microgrid is obtained and the active and reactive power outputs P_s, Q_s of the BESS are calculated via the power calculation

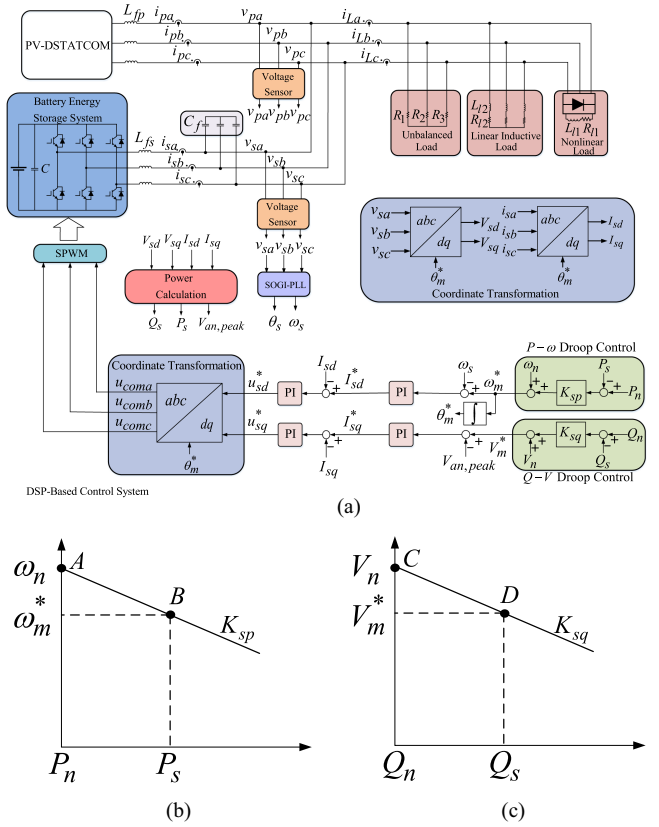

Fig. 2. Schematic diagram of BESS. (a) Control block of BESS with droop control. (b) $P-\omega$ droop characteristic. (c) $Q-V$ droop characteristic.

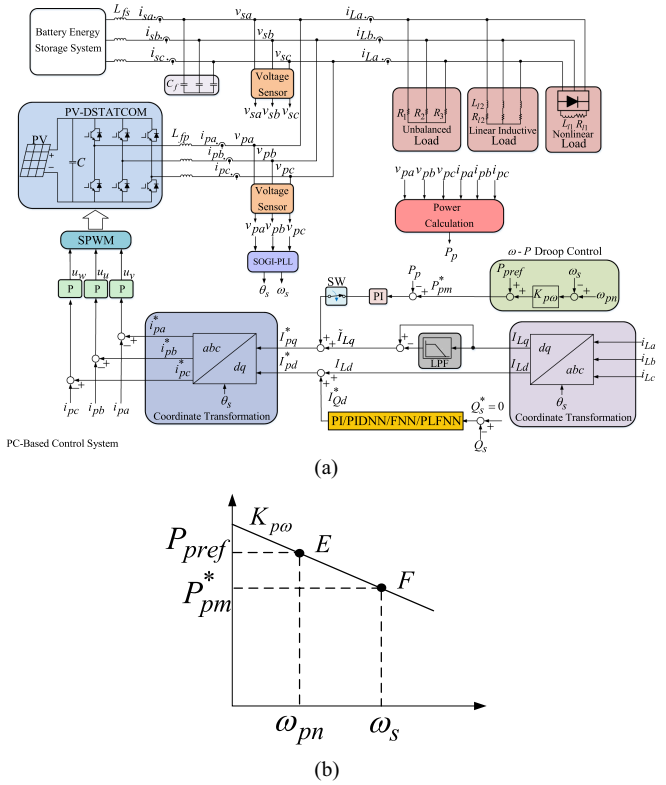

Fig. 3. Schematic diagram of PV-DSTATCOM. (a) Control block of PV-DSTATCOM with droop control. (b) $\omega-P$ droop characteristic.

as follows:

$$\begin{bmatrix} P_s \\ Q_s \end{bmatrix} = \frac{3}{2} \begin{bmatrix} V_{sd} & V_{sq} \\ -V_{sq} & V_{sd} \end{bmatrix} \begin{bmatrix} I_{sd} \\ I_{sq} \end{bmatrix}. \tag{1}$$

In addition, the $P-\omega$ and Q–V droop characteristics of the BESS shown in Fig. 2(b) and (c), respectively, are described as follows [2], [10]:

$$\omega_m^* = \omega_n + K_{sp}(P_n - P_s) \tag{2}$$

$$V_m^* = V_n + K_{sq}(Q_n - Q_s) \tag{3}$$

where the reference angular frequency ω_n is set to be 377 rad/s at no load; the reference amplitude of phase voltage V_n is set to be 89.8 V at no load; the droop coefficients K_{sp} and K_{sq} are set to be 0.002167 (rad/s)/W and 0.05 V/Var; the reference active power P_n and reactive power Q_n are set to be zero. By means of the integral operation with the angular frequency command ω_m^* shown in (2), the electric angle θ_m^* can be acquired for the coordinate transformation. Generally, the electric angle θ_s will be equal to θ_m^*. Afterward, the frequency error $\omega_m^* - \omega_s$ and the voltage error $V_m^* - V_{an,peak}$ are transmitted to the PI controllers to obtain the dq-axis current commands I_{sd}^*, I_{sq}^*. Accordingly, the errors between the dq-axis current commands I_{sd}^*, I_{sq}^* and the dq-axis current components I_{sd}, I_{sq} are sent to two PI controllers and an inverse coordinate transformation is adopted to obtain the three-phase reference commands u_{coma}, u_{comb}, u_{comc}. Finally, the switching signals of the insulated gate bipolar transistor (IGBT) are obtained via the sinusoidal pulsewidth modulation (SPWM). Consequently, the object of the BESS with the droop control can be achieved.

B. Control Scheme of PV-DSTATCOM

A PV-DSTATCOM with novel control scheme is developed to overcome the power quality issues in the droop controlled microgrid. The novel control scheme of the developed PV-DSTATCOM owns the $\omega-P$ droop characteristic and the ability of the DSTATCOM to compensate the reactive power for the power quality improvement and voltage support. The schematic diagram of the developed PV-DSTATCOM is represented in Fig. 3. The control block of the PV-DSTATCOM with droop control is illustrated in Fig. 3(a). The $\omega-P$ droop characteristic adopted in the developed PV-DSTATCOM is given in Fig. 3(b). First, the SOGI-PLL is also adopted in the PV-DSTATCOM to obtain ω_s and θ_s. The acquired ω_s and θ_s are adopted for the droop control and coordinate transformation, respectively. Moreover, the three-phase voltages v_{pa}, v_{pb}, v_{pc} and three-phase currents i_{pa}, i_{pb}, i_{pc} of the PV-DSTATCOM are detected to calculate the active power P_P of the PV-DSTATCOM as shown in Fig. 3(a). Afterward, the dq-axis load currents I_{Ld}, I_{Lq} are computed by using the obtained three-phase load currents i_{La}, i_{Lb}, i_{Lc} via the abc/dq coordinate transformation. Because the dq-axis load currents I_{Ld}, I_{Lq} consist of the dc current components $\bar{I}_{Ld}, \bar{I}_{Lq}$ and ac current components $\tilde{I}_{Ld}, \tilde{I}_{Lq}$, a low pass filter is adopted in q-axis load current I_{Lq} to extract the dc current component $\bar{I}_{Lq}$, and then subtracted from

I_{Lq} to obtain the ac current component $\tilde{I}_{Lq}$. Furthermore, to implement the droop control in the developed PV-DSTATCOM, the $\omega-P$ droop characteristic shown in Fig. 3(b) is adopted to dispatch the corresponding active power according to the power demand of the loads and is described as follows:

$$P_{pm}^{*} = P_{pref} + K_{p\omega}(\omega_{pn} - \omega_s) \tag{4}$$

where the reference active power P_{pref} is set to be 1600 W; the droop coefficient $K_{p\omega}$ is set to be 307.6923 W/(rad/s); the reference angular frequency ω_{pn} is set to be 371.8 rad/s. In this article, when the solar irradiation is sufficient for the PV-DSTATCOM to generate the required P_P, the switch (SW) shown in Fig. 3(a) turns on to dispatch the corresponding active power according to (4) for power sharing. The active power error $P_{pm}^{*} - P_p$ is transmitted to the PI controller and is added to the ac current component $\tilde{I}_{Lq}$ to obtain the q-axis current command I_{pq}^{*}. On the other hand, when the solar irradiation isn't sufficient and the computed active power P_P of the PV-DSTATCOM is less than the active power command P_{pm}^{*}, the SW will turn OFF. Therefore, the q-axis current command I_{pq}^{*} will be equal to the ac current component $\tilde{I}_{Lq}$. In addition, to achieve the reactive power compensation of the DSTATCOM for the power quality improvement and voltage support, the reactive power error $Q_s^{*} - Q_s$ of the BESS is sent to the PI, proportional–integral–derivative neural network (PIDNN) [37], FNN or the proposed PLFNN controller to generate the d-axis reactive power command I_{Qd}^{*}. Then, the d-axis reactive power command I_{Qd}^{*} is added to the d-axis load current I_{Ld} to acquire the d-axis current command I_{pd}^{*}. Additionally, the three-phase reference commands u_u, u_v, u_w for generating the switching signals of the IGBT via the SPWM are computed by means of three-phase current control and coordinate transformation using dq-axis current commands I_{pd}^{*} and I_{pq}^{*}. Finally, the objective of the developed PV-DSTATCOM with the $\omega-P$ droop characteristic and the ability of the DSTATCOM to compensate the reactive power for the power quality improvement and voltage support can be achieved.

In this article, since the dq-axis ac current components $\tilde{I}_{Ld}, \tilde{I}_{Lq}$ correspond to the harmonic load currents in abc frame, the current harmonics can be eliminated by using the dq-axis ac current components $\tilde{I}_{Ld}, \tilde{I}_{Lq}$ of the PV-DSTATCOM. On the other hand, the PF correction is mainly implemented by the d-axis reactive power command I_{Qd}^{*} for the reactive power compensation. Moreover, since the current harmonics are resulted from the nonlinear load composed of a full-bridge rectifier with inductor L_{l1} and resistor R_{l1} as shown in Fig. 3(a), the d-axis reactive power command I_{Qd}^{*} for the reactive power compensation will also mitigate the reactive power demanded from the inductor L_{l1} and the resulted current harmonics. Consequently, the dq-axis current commands I_{pd}^{*} and I_{pq}^{*} of the PV-DSTATCOM can effectively improve the current THD and correct the PF in the droop controlled microgrid. Furthermore, when the insufficient solar irradiation occurs, the PV-DSTATCOM still owns the abilities of the DSTATCOM in accordance with the control scheme to reduce the current THD, correct PF, compensate the reactive power for voltage support, and mitigate the three-phase unbalanced system currents of the microgrid.

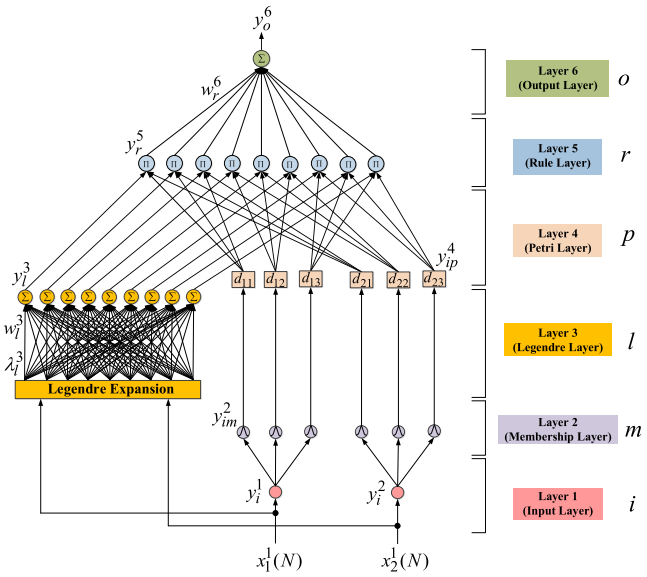

Fig. 4. Network structure of proposed PLFNN controller.

III. Online Trained PLFNN Controller

In this article, to enhance the power quality of the droop controlled microgrid and solve the drawbacks of the conventional PI controller, a novel PLFNN controller is proposed for the PV-DSTATCOM to replace the PI controller. The network structure of the proposed PLFNN controller is given in Fig. 4. The PLFNN controller comprises the input layer, membership layer, Legendre layer, Petri layer, rule layer and the output layer. The detailed derivation of the network structure and online learning algorithm of the proposed PLFNN controller is described as later. Moreover, the flowchart of PV-DSTATCOM using the proposed PLFNN controller for reactive power compensation is described in Appendix.

A. Network Structure

The relationship between the layers in the developed PLFNN controller is expressed in the following.

1) Input Layer: The signal transduction in this layer is depicted as

$$\text{net}_i^1(N) = x_i^1(N) \tag{5}$$

$$y_i^1(N) = f_i^1(\text{net}_i^1(N)) = \text{net}_i^1(N) \qquad i = 1, 2 \tag{6}$$

where N signifies the Nth iteration; $x_i^1(\text{N})$ exhibits the ith input to the input layer. In this article, the inputs of the developed PLFNN controller are the reactive power error $x_1^1(N) = e = Q_s^{*} - Q_s$ of the BESS and its corresponding derivative $x_2^1(N) = \dot{e}$ as shown in Fig. 3(a).

2) Membership Layer: The fuzzification operation is executed by means of the Gaussian functions in this layer. The input information is mapped to a membership degree between 0 and 1 as

$$\text{net}_{im}^2(N) = -\frac{\left(y_i^1(N) - m_{im}^2(N)\right)^2}{\left(\sigma_{im}^2(N)\right)^2} \tag{7}$$

$$y_{im}^2(N) = f_{im}^2(\text{net}_{im}^2(N)) = \exp(\text{net}_{im}^2(N)), m = 1,\ 2,\ 3. \tag{8}$$

The outputs of the nodes to represent the membership degree are $y_{im}^2(N)$.

3) Legendre Layer: The Legendre polynomials are a set of completely orthogonal polynomials and can expand the original input vector with faster convergence rate [32]. Hence, the Legendre polynomials are utilized as the functional expansion functions. The vector of the input variables $x = [x_1^1, x_2^1]$ can be separated in the enhanced space in the following [32]:

$$\begin{aligned}\lambda &= [\lambda_1^3, \lambda_2^3, \ldots,\ \lambda_l^3]^T \\ &= [L_0, L_1(x_1^1), L_2(x_1^1), L_3(x_1^1), L_4(x_1^1) \\ &\quad L_1(x_2^1), L_2(x_2^1), L_3(x_2^1), L_4(x_2^1)]^T\end{aligned} \tag{9}$$

where λ_l^3 is the output of the Legendre expansion; λ is the vector output of the Legendre expansion; $L_h(x)$ stand for the Legendre polynomials, in which $-1 < x < 1$ depicts the argument of the polynomial and h represents the order of the expansion. The signal transduction in Legendre layer is described as

$$\text{net}_l^3(N) = \sum_{l=1}^{9} w_l^3 \lambda_l^3(N) \tag{10}$$

$$y_l^3(N) = f_l^3(\text{net}_l^3(N)) = \text{net}_l^3(N). \tag{11}$$

4) Petri Layer: The competition principle to select the suitable fired node is utilized in Petri layer for the main objective of generating the tokens. Once the token is generated at the input place, the transition becomes enabled state. Consequently, the state of the transition, whether fired or unfired, is expressed as

$$t_{ip}^4(N) = \begin{cases} 1, & y_{im}^2(N) \geq d_{ip} \\ 0, & y_{im}^2(N) < d_{ip} \end{cases}, \quad p = 1, 2, 3 \tag{12}$$

$$d_{ip} = \frac{\alpha \exp(-\beta H)}{1 + \exp(-\beta H)} \tag{13}$$

$$H = \frac{1}{2}(e + \dot{e}). \tag{14}$$

Moreover, the signal transduction of the nodes in Petri layer is described in the following:

$$\text{net}_{ip}^4(N) = y_{im}^2(N) t_{ip}^4(N) \tag{15}$$

$$y_{ip}^4(N) = f_{ip}^4(\text{net}_{ip}^4(N)) = \text{net}_{ip}^4(N). \tag{16}$$

5) Rule Layer: In rule layer, the multiplication operation is carried out to obtain the product of the input data. The relationship between the input and the output of rule layer is depicted as

$$\text{net}_r^5(N) = \prod_l y_l^3 y_{1p}^4 y_{2p}^4 \tag{17}$$

$$y_r^5(N) = f_r^5(\text{net}_r^5(N)), \quad r = 1,\ 2, \ldots,\ 9. \tag{18}$$

6) Output Layer: In output layer, the summation operation is utilized to carry out the defuzzification process. Therefore, the signal transduction of this layer is given as

$$\text{net}_o^6(N) = \sum_{r=1}^{9} w_r^6 y_r^5(N), \quad o = 1 \tag{19}$$

$$y_o^6(N) = f_o^6(\text{net}_o^6(N)) = \text{net}_o^6(N) \tag{20}$$

where $y_o^6(N)$ is the output of the proposed PLFNN controller for the developed PV-DSTATCOM, which is a part of the d-axis current command I_{pd}^* as shown in Fig. 3(a) to effectively compensate the reactive power for the power quality improvement and voltage support.

B. Online Learning Algorithm

In accordance with the supervised learning strategy, the parameter learning is accomplished through the online tuning of the connected weights between the output layer and rule layer, the connected weights in Legendre layer, and the mean and standard deviation of the membership functions using the backpropagation (BP) strategy for minimizing a given error function E, which is defined as

$$E(N) = \frac{1}{2}(Q_s^* - Q_s)^2 = \frac{1}{2}e^2. \tag{21}$$

The derivation of the online learning algorithm of the proposed PLFNN controller for the PV-DSTATCOM is described in detail as follows:

1) Output Layer: The error term of the output layer is propagated as

$$\delta_o^6 = -\frac{\partial E(N)}{\partial y_o^6(N)} = -\frac{\partial E(N)}{\partial Q_s}\frac{\partial Q_s}{\partial y_o^6(N)}. \tag{22}$$

The connected weight is computed and updated in the following by using the chain rule

$$\Delta w_r^6 = -\eta_r \frac{\partial E(N)}{\partial w_r^6} = -\eta_r \frac{\partial E(N)}{\partial y_o^6(N)}\frac{\partial y_o^6(N)}{\partial w_r^6(N)} = \eta_r \delta_o^6 y_r^5(N). \tag{23}$$

The connected weight w_r^6 will be updated as

$$w_r^6(N+1) = w_r^6(N) + \Delta w_r^6. \tag{24}$$

2) Rule Layer: In rule layer, the error terms to be propagated are derived as

$$\delta_r^5 = -\frac{\partial E(N)}{\partial y_r^5(N)} = -\frac{\partial E(N)}{\partial y_o^6(N)}\frac{\partial y_o^6(N)}{\partial y_r^5(N)} = \delta_o^6 w_r^6(N). \tag{25}$$

3) Legendre Layer: The term of the propagated error is calculated as

$$\begin{aligned}\delta_l^3 &= -\frac{\partial E(N)}{\partial y_l^3(N)} = -\frac{\partial E(N)}{\partial y_o^6(N)}\frac{\partial y_o^6(N)}{\partial y_r^5(N)}\frac{\partial y_r^5(N)}{\partial y_l^3(N)} \\ &= \delta_r^5 y_{1p}^4 y_{2p}^4(N).\end{aligned} \tag{26}$$

In accordance with the chain rule, the update of the connected weight Δw_l^3 is derived as

$$\Delta w_l^3 = -\eta_l \frac{\partial E(N)}{\partial w_l^3(N)}$$

$$= -\eta_l \frac{\partial E(N)}{\partial y_o^6(N)} \frac{\partial y_o^6(N)}{\partial y_r^5(N)} \frac{\partial y_r^5(N)}{\partial y_l^3(N)} \frac{\partial y_l^3(N)}{\partial w_l^3(N)}$$

$$= \eta_l \delta_l^3 \lambda_l^3(N). \tag{27}$$

Thus, the updated connected weight w_l^3 is computed as

$$w_l^3(N+1) = w_l^3(N) + \Delta w_l^3. \tag{28}$$

4) Membership Layer: By using the chain rule, the error term needs to be computed and propagated as

$$\delta_{im}^2 = -\frac{\partial E(N)}{\partial \text{net}_{im}^2(N)}$$

$$= -\frac{\partial E(N)}{\partial y_o^6(N)} \frac{\partial y_o^6(N)}{\partial y_r^5(N)} \frac{\partial y_r^5(N)}{\partial y_{im}^2(N)} \frac{\partial y_{im}^2(N)}{\partial \text{net}_{im}^2(N)}$$

$$= \sum \delta_r^5 y_r^5(N). \tag{29}$$

The updates of the standard deviation $\Delta\sigma_{im}^2$ and mean Δm_{im}^2 of the membership functions are derived in the following:

$$\Delta\sigma_{im}^2 = -\eta_\sigma \frac{\partial E(N)}{\partial \sigma_{im}^2(N)}$$

$$= -\eta_\sigma \frac{\partial E(N)}{\partial y_o^6(N)} \frac{\partial y_0^6(N)}{\partial y_r^5(N)} \frac{\partial y_r^5(N)}{\partial y_{im}^2(N)} \frac{\partial y_{im}^2(N)}{\partial \text{net}_{im}^2(N)} \frac{\partial \text{net}_{ij}^2(N)}{\partial \sigma_{ij}^2(N)}$$

$$= \eta_\sigma \delta_{im}^2 \frac{2(y_i^1 - m_{im}^2)^2}{(\sigma_{im}^2)^3} \tag{30}$$

$$\Delta m_{im}^2 = -\eta_m \frac{\partial E(N)}{\partial m_{im}^2(N)}$$

$$= -\eta_m \frac{\partial E(N)}{\partial y_o^6(N)} \frac{\partial y_0^6(N)}{\partial y_r^5(N)} \frac{\partial y_r^5(N)}{\partial y_{im}^2(N)} \frac{\partial y_{im}^2(N)}{\partial net_{im}^2(N)} \frac{\partial \text{net}_{im}^2(N)}{\partial m_{im}^2(N)}.$$

$$= \eta_m \delta_{im}^2 \frac{2(y_i^1 - m_{im}^2)}{(\sigma_{im}^2)^2} \tag{31}$$

Consequently, the updated standard deviation σ_{im}^2 and mean m_{im}^2 of the membership functions are calculated as

$$\sigma_{im}^2(N+1) = \sigma_{im}^2(N) + \Delta\sigma_{im}^2 \tag{32}$$

$$m_{im}^2(N+1) = m_{im}^2(N) + \Delta m_{im}^2. \tag{33}$$

On account of the uncertainties such as the parameter variations and external disturbances in the droop controlled microgrid, the calculation of the Jacobian of the droop controlled microgrid, $\partial Q_s/\partial y_o^6(N)$, is hard to obtain accurately. Hence, for the purposes of overcoming this issue and increasing the online learning rate of the network parameters, the delta adaptation law is utilized as follows [3], [10]:

$$\delta_o^6 \cong (Q_s^* - Q_s) + (\dot{Q}_s^* - \dot{Q}_s) = e + \dot{e}. \tag{34}$$

IV. Design and Experimentation

The developed droop controlled microgrid is provided in Fig. 5. The block diagrams of the BESS and the developed PV-DSTATCOM using the proposed PLFNN controller for the power quality improvement and voltage support are illustrated in Fig. 5(a) and (b), respectively. In this article, the BESS is

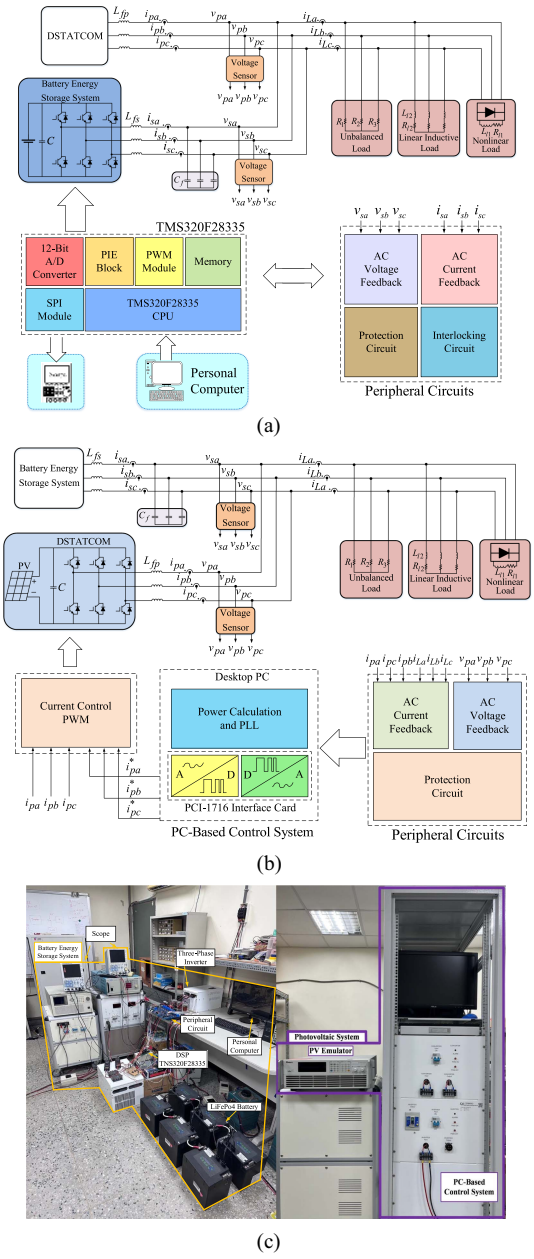

Fig. 5. Developed droop controlled microgrid. (a) Block diagram of BESS. (b) Block diagram of PV-DSTATCOM. (c) Photos of experimental setup.

controlled by a TMS320F28335 digital signal processor-based control system with the sampling frequency 1 kHz and switching frequency 16 kHz as shown in Fig. 5(a). The three-phase voltages v_{sa}, v_{sb}, v_{sc} and three-phase currents i_{sa}, i_{sb}, i_{sc} of the BESS are detected and set to the peripheral circuits for the implementations of the SOGI-PLL, $P-\omega$ and Q-V droop controls. Moreover, a personal computer (PC) based control platform is utilized to implement the PV-DSTATCOM through the MATLAB & Simulink real-time control package with the sampling frequency 2 kHz (0.5 ms sampling time) and switching frequency 10 kHz. The three-phase voltages v_{pa}, v_{pb}, v_{pc} and currents i_{pa}, i_{pb}, i_{pc} of the PV-DSTATCOM and the three-phase

TABLE I
SYSTEM PARAMETERS OF DEVELOPED MICROGRID

Parameters	Values
DC Voltage of BESS	237.6 V
DC-Link Capacitor : C	2200 μF
Filter Inductor of BESS: L_{fs}	3 mH
Filter Inductor of PV-DSTATCOM: L_{fp}	10 mH
Filter Capacitor : C_f	46 μF
Switching Frequency of BESS	16 kHz
Outer Sampling Frequency of BESS	1 kHz
Sampling Frequency of BESS	16 kHz
Switching Frequency of PV-DSTATCOM	10 kHz
Sampling Frequency of PV-DSTATCOM	2 kHz

load currents i_{La}, i_{Lb}, i_{Lc} are acquired and transmitted to the control platform for the implementations of the proposed PLFNN controller, SOGI-PLL, $\omega - P$ droop control and reactive power compensation for the power quality improvement and voltage support. In the experimentation, in order to verify the effectiveness of the PV-DSTATCOM, the solar irradiation is assumed to be sufficient. The BESS is also 80% charged. Furthermore, the photos of the experimental setup are given in Fig. 5(c). In addition, the detailed system parameters of the developed microgrid are provided in Table I.

In this article, the loads consist of a nonlinear load, an unbalanced load and a linear inductive load to generate the deteriorated current harmonics, unbalanced system currents, and lagging PF. Hence, to certify the effectiveness of the developed PV-DSTATCOM using the proposed PLFNN controller to reduce the current THD, correct PF, compensate the reactive power for voltage support, and mitigate the three-phase unbalanced system currents, two test scenarios of the loads are designed. In case 1, the loads are composed of the nonlinear load, which is a full-bridge rectifier with $L_{l1} = 1$ mH and $R_{l1} = 75\ \Omega$ as shown in Fig. 5(a), the unbalanced load $R_1 = 80\ \Omega$, $R_2 = 40\ \Omega$ and $R_3 = 160\ \Omega$, and the linear inductive load $R_{l2} = 25\ \Omega$ and $L_{l2} = 50$ mH. In case 2, the loads still comprise the unbalanced load $R_1 = 80\ \Omega$; $R_2 = 40\ \Omega$; $R_3 = 160\ \Omega$, and the linear inductive load $R_{l2} = 25\ \Omega$; $L_{l2} = 50$ mH with rapid change of the nonlinear load. The nonlinear load is changed from $L_{l1} = 1$ mH; $R_{l1} = 100\ \Omega$ to $L_{l1} = 1$ mH; $R_{l1} = 33\ \Omega$, and finally changed to $L_{l1} = 1$ mH; $R_{l1} = 75\ \Omega$. Moreover, to demonstrate the compensation performance of the developed PV-DSTATCOM, a three-phase current unbalanced ratio (CUR) is defined as

$$\text{CUR} = \frac{\text{Max}(i_{sa},\ i_{sb},\ i_{sc}) - \text{Min}(i_{sa},\ i_{sb},\ i_{sc})}{\text{Avg}(i_{sa},\ i_{sb},\ i_{sc})} 100\% \quad (35)$$

where $\text{Max}(i_{sa}, i_{sb}, i_{sc})$, $\text{Min}(i_{sa}, i_{sb}, i_{sc})$ and $\text{Avg}(i_{sa}, i_{sb}, i_{sc})$ symbolize the maximum, minimum and average RMS currents of the three-phase currents i_{sa}, i_{sb}, i_{sc} of the BESS. The lesser value the CUR is, the better balanced three-phase system currents the developed PV-DSTATCOM owns. Furthermore, the experimental results of the PV-DSTATCOM using the PI, PIDNN, FNN, and the proposed PLFNN controllers are given for the comparison of control performance.

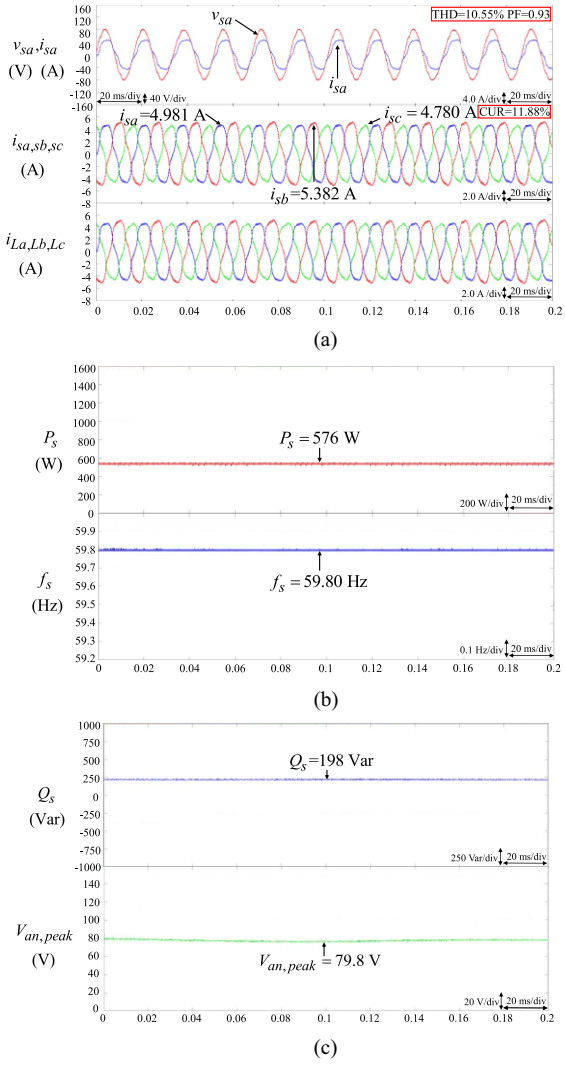

Fig. 6. Experimental results without using PV-DSTATCOM at case 1. (a) Responses of voltage v_{sa}, current i_{sa}, three-phase currents i_{sa}, i_{sb}, i_{sc} of BESS, and three-phase load currents i_{La}, i_{Lb}, i_{Lc}. (b) Responses of active power P_s of BESS and frequency f_s of microgrid. (c) Responses of reactive power Q_s of BESS and voltage $V_{an,peak}$ of microgrid.

The test scenario at case 1 is demonstrated first. To compare the performance of the PV-DSTATCOM for the power quality improvement and voltage support, the experimental results without using the PV-DSTATCOM are also provided in Fig. 6 for demonstration. The responses of the phase-a voltage v_{sa}, current i_{sa}, three-phase currents i_{sa}, i_{sb}, i_{sc} of the BESS, and the three-phase load currents i_{La}, i_{Lb}, i_{Lc} are given in Fig. 6(a). The responses of the active power P_s of the BESS and the frequency f_s of the droop controlled microgrid are represented in Fig. 6(b). The responses of the reactive power Q_s of the BESS and the peak value of the phase voltage $V_{an,peak}$ are presented in Fig. 6(c). From the experimental result as shown in Fig. 6(a), because the dirty loads exist in the microgrid, the current distortion i_{sa} of the BESS is very serious and obvious. Moreover, the current i_{sa} of the BESS is severely lagged the voltage v_{sa}. Thus, the

current THD and lagging PF are 10.55% and 0.93, respectively. Then, the high value 11.88% of the CUR means the severe unbalanced currents resulted in the deteriorated power quality. Furthermore, according to Fig. 6(b) and (c), since the BESS adopted the $P-\omega$ and Q − V droop controls, the frequency and voltage of the microgrid are self-regulated to be 59.8 Hz and 79.8 V to dispatch the corresponding active power $P_s = 576$ W and reactive power $Q_s = 198$ Var of the BESS, respectively, in accordance with the power demand of the loads. Consequently, the droop characteristics of the BESS can be achieved. Then, the experimental results using the PI-based PV-DSTATCOM at case 1 are illustrated in Fig. 7. The responses of the phase-a voltage v_{sa}, current i_{sa}, three-phase currents i_{sa}, i_{sb}, i_{sc} of the BESS, and the three-phase load currents i_{La}, i_{Lb}, i_{Lc} are given in Fig. 7(a). The responses of the active power P_s of the BESS and the frequency f_s of the droop controlled microgrid are represented in Fig. 7(b). The responses of the reactive power Q_s of the BESS and the phase voltage $V_{an,peak}$ are provided in Fig. 7(c). The responses of active and reactive powers P_P, Q_P of the developed PV-DSTATCOM are shown in Fig. 7(d). In accordance with Fig. 7(a) and (b), since the PV-DSTATCOM is adopted in the droop controlled microgrid, the current THD can be improved to be 4.48%, which complies with the international standard within 5%. In other words, the current is almost sinusoidal. The PF and the CUR are also improved to be 0.99 and 2.21%, respectively. The frequency of the microgrid is self-regulated to 59.85 Hz as shown in Fig. 7(b). Thus, the power quality can be improved by using the PV-DSTATCOM. In addition, from the experimental results as shown in Fig. 7(c) and (d), since the PV-DSTATCOM can dispatch the reactive power not only for the power quality improvement but also the voltage support, the phase voltage $V_{an,peak}$ of the microgrid is recovered to be 89.8 V and the reactive power Q_s of the BESS is reduced to be 0 Var according to the $Q-V$ droop characteristic of the BESS. Then, the PV-DSTATCOM can also dispatch the active power $P_P = 298$ W for the power demand of the loads according to the $\omega-P$ droop characteristic of the PV-DSTATCOM. Hence, the performance of the PV-DSTATCOM to own the $\omega-P$ droop characteristic and the abilities of the DSTATCOM for the power quality improvement and voltage support is verified. Additionally, the experimental results using the PIDNN-based, FNN-based and the PLFNN-based PV-DSTATCOM at case 1 are represented in Figs. 8–10, respectively. From the experimental results shown in Figs. 8(a)–10(a), since the proposed PLFNN controller possesses the capabilities of PFNN to approximate, learn and optimize the dynamic system, to cope with the uncertain information, and the capability of Legendre polynomials to expand the original input vector with faster convergence rate, the current THD, PF and CUR are mush improved to be 2.84%, 0.99 and 1.04%, which are superior to the PIDNN-based PV-DSTATCOM with 4.39%, 0.99 and 2.13% and FNN-based PV-DSTATCOM with 4.23%, 0.99 and 1.91%. Additionally, the current THD, PF and CUR of the PV-DSTATCOM using the PI, PIDNN, FNN and the proposed PLFNN controllers at case 1 are given in Table II. According to the experimental results shown in Figs. 6–10 and Table II, the performance of the PV-DSTATCOM with $\omega-P$ droop characteristic and the abilities of the power quality improvement and voltage support is verified. Moreover, the superior power quality improvement is certified by using the proposed PLFNN controller owing to the powerful robust control ability compared with the PI, PIDNN and FNN controllers.

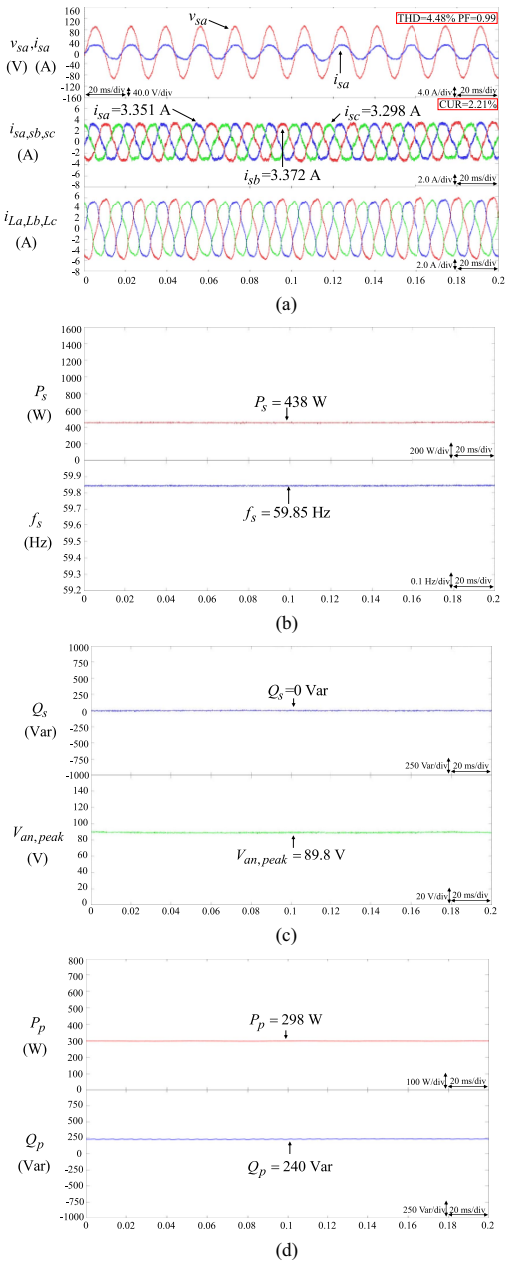

Fig. 7. Experimental results using PI-based PV-DSTATCOM at case 1. (a) Responses of voltage v_{sa}, current i_{sa}, three-phase currents i_{sa}, i_{sb}, i_{sc} of BESS, and three-phase load currents i_{La}, i_{Lb}, i_{Lc}. (b) Responses of active power P_s of BESS and frequency f_s of microgrid. (c) Responses of reactive power Q_s of BESS and voltage $V_{an,peak}$ of microgrid. (d) Responses of active and reactive powers P_P, Q_P of PV-DSTATCOM.

The external disturbance such as the load change for the PI, PIDNN, FNN, and the proposed PLFNN controllers is demonstrated at case 2. The nonlinear load is changed from $L_{l1} = 1$ mH; $R_{l1} = 100\ \Omega$ to $L_{l1} = 1$ mH; $R_{l1} = 33\ \Omega$, and finally changed to $L_{l1} = 1$ mH; $R_{l1} = 75\ \Omega$ at 1.5 s and 3.5 s. Firstly,

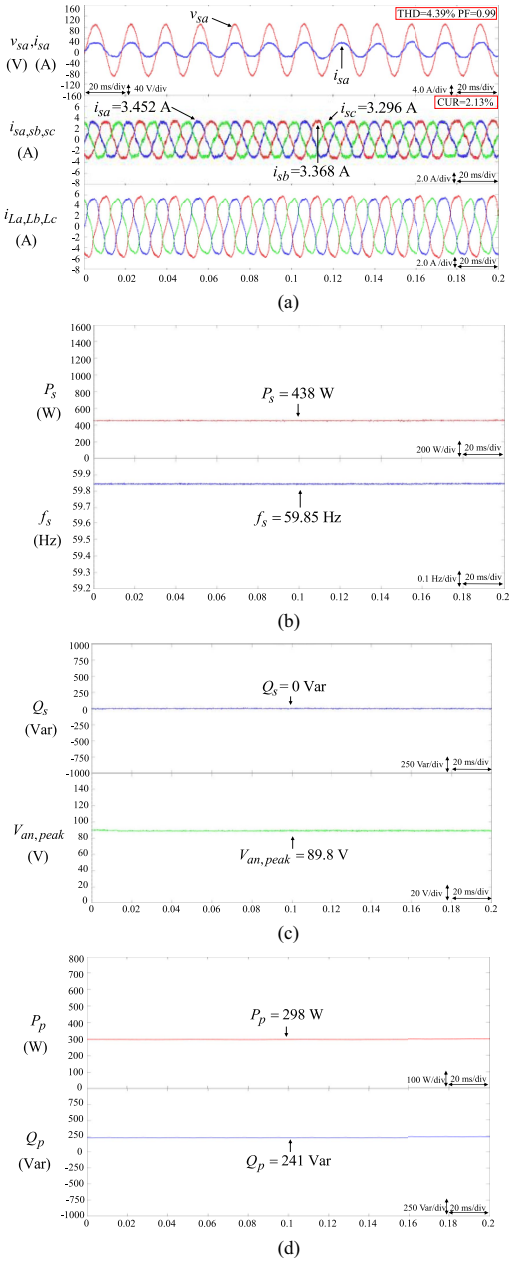

Fig. 8. Experimental results using PIDNN-based PV-DSTATCOM at case 1. (a) Responses of voltage v_{sa}, current i_{sa}, three-phase currents i_{sa}, i_{sb}, i_{sc} of BESS, and three-phase load currents i_{La}, i_{Lb}, i_{Lc}. (b) Responses of active power P_s of BESS and frequency f_s of microgrid. (c) Responses of reactive power Q_s of BESS and voltage $V_{an,peak}$ of microgrid. (d) Responses of active and reactive powers P_P, Q_P of PV-DSTATCOM.

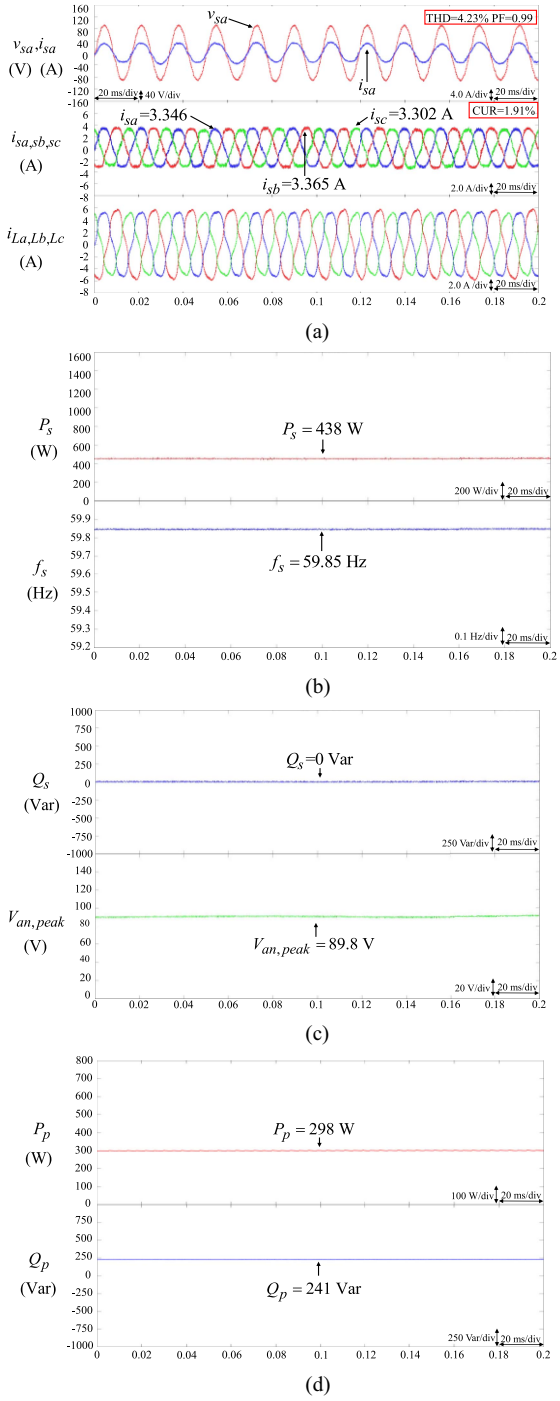

Fig. 9. Experimental results using FNN-based PV-DSTATCOM at case 1. (a) Responses of voltage v_{sa}, current i_{sa}, three-phase currents i_{sa}, i_{sb}, i_{sc} of BESS, and three-phase load currents i_{La}, i_{Lb}, i_{Lc}. (b) Responses of active power P_s of BESS and frequency f_s of microgrid. (c) Responses of reactive power Q_s of BESS and voltage $V_{an,peak}$. (d) Responses of active and reactive powers P_P, Q_P of PV-DSTATCOM.

the experimental result without using the PV-DSTATCOM is also given in Fig. 11 for comparison. The responses of the active power P_s of the BESS and the frequency f_s of the microgrid are provided in Fig. 11(a). The responses of the reactive power Q_s of the BESS and the phase voltage $V_{an,peak}$ are shown in Fig. 11(b). From the experimental result as shown in Fig. 11(a), since the nonlinear load is changed at 1.5 and 3.5 s, the frequency f_s of the microgrid is changed from 59.82 to 59.76 Hz, and finally changed to 59.8 Hz for dispatching the corresponding active power P_s of the BESS according to the adopted $P-\omega$ control of the BESS. The corresponding active powers P_s of the BESS are 537, 810, and 583 W. The settling time of the active power P_s is 523 and 447 ms, respectively. Then, because of the absence of the PV-DSTATCOM for the reactive power compensation to achieve the voltage support, the phase voltage $V_{an,peak}$ is changed form 80.3 V to 77.2 V and finally changed to 79.8 V. The reactive

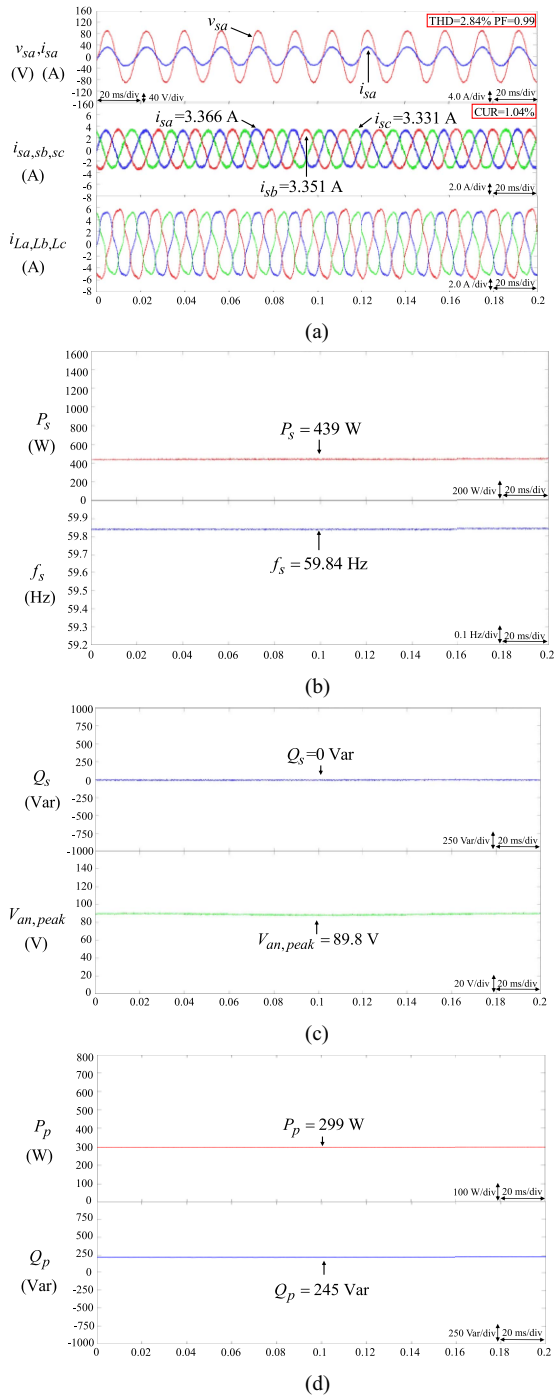

Fig. 10. Experimental results using PLFNN-based PV-DSTATCOM at case 1. (a) Responses of voltage v_{sa}, current i_{sa}, three-phase currents i_{sa}, i_{sb}, i_{sc} of BESS, and three-phase load currents i_{La}, i_{Lb}, i_{Lc}. (b) Responses of active power P_s of BESS and frequency f_s of microgrid. (c) Responses of reactive power Q_s of BESS and voltage $V_{an,peak}$. (d) Responses of active and reactive powers P_P, Q_P of PV-DSTATCOM.

power Q_s of the BESS is also self-regulated from 193 Var to 251 Var, and finally changed to 204 Var as shown in Fig. 11(b) according to the adopted Q − V droop control of the BESS. The maximum reactive power Q_s error and phase voltage $V_{an,peak}$ error are 175 Var and 19 V. Consequently, the voltage support and system reliability of the microgrid are poor. Moreover, the

TABLE II
CURRENT THD, PF, AND CUR OF PV-DSTATCOM USING PI, PIDNN, FNN AND PLFNN CONTROLLERS AT CASE 1

Case Conditions	Controllers	Current THD	PF	CUR
Case 1	None	10.55 %	0.92	11.88 %
	PI	4.48 %	0.99	2.21 %
	PIDNN	4.39 %	0.99	2.13 %
	FNN	4.23 %	0.99	1.91 %
	PLFNN	2.84 %	0.99	1.04 %

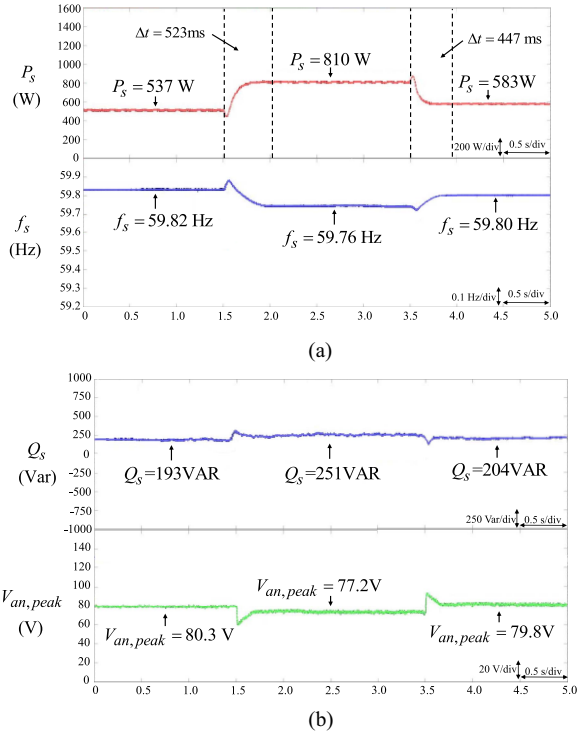

Fig. 11. Experimental results without using PV-DSTATCOM at case 2. (a) Responses of active power P_s of BESS and frequency f_s of microgrid. (b) Responses of reactive power Q_s of BESS and voltage $V_{an,peak}$.

experimental results using the PI-based PV-DSTATCOM at case 2 are represented in Fig. 12. The responses of the active power P_s of the BESS and the frequency f_s of the microgrid are presented in Fig. 12(a). The responses of the reactive power Q_s of the BESS and the phase voltage $V_{an,peak}$ are illustrated in Fig. 12(b). The responses of the active and reactive powers P_P, Q_P of the PV-DSTATCOM are provided in Fig. 12(c). From the experimental result shown in Fig. 12(a), when the load changes at 1.5 and 3.5 s, respectively, the frequency f_s of the microgrid is changed from 59.86 to 59.78 Hz, and finally changed to 59.84 Hz for dispatching the corresponding active power P_s of the BESS according to the power demand of the loads. Nevertheless, since the poor control property of the PI controller couldn't effectively deal with the external disturbances, the response of the PI-based PV-DSTATCOM to compensate the reactive power is sluggish as shown in Fig. 12(c) and it results in the obvious fluctuations in the

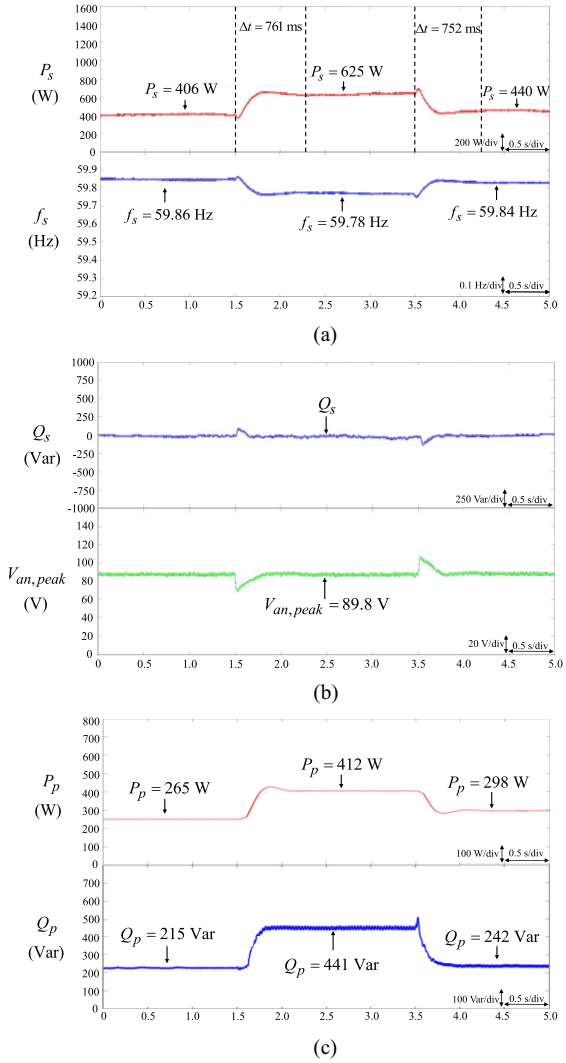

Fig. 12. Experimental results using PI-based PV-DSTATCOM at case 2. (a) Responses of active power P_s of BESS and frequency f_s of microgrid. (b) Responses of reactive power Q_s of BESS and voltage $V_{an,peak}$. (c) Responses of active and reactive powers P_P, Q_P of PV-DSTATCOM.

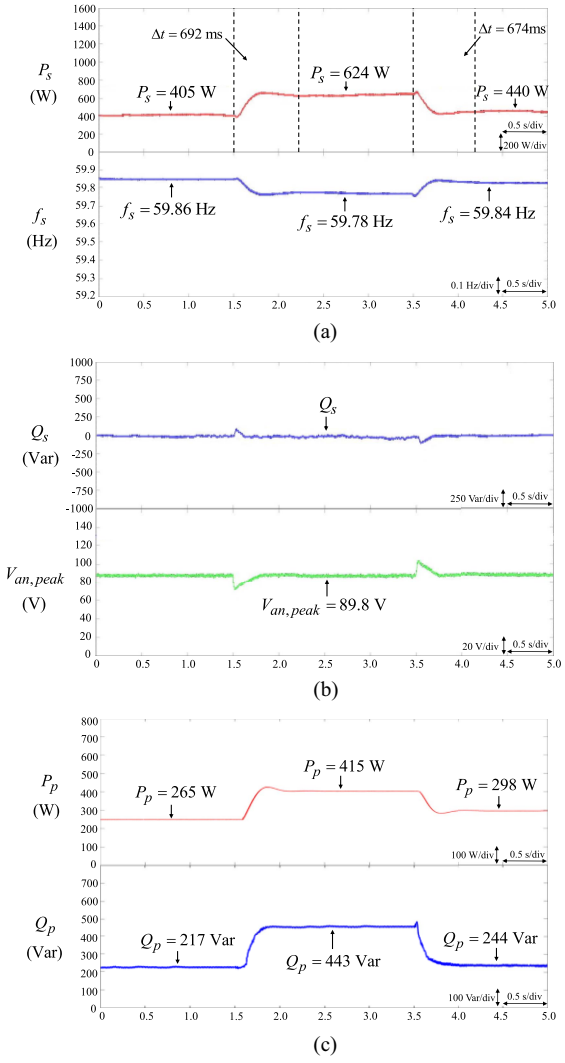

Fig. 13. Experimental results using PIDNN-based PV-DSTATCOM at case 2. (a) Responses of active power P_s of BESS and frequency f_s of microgrid. (b) Responses of reactive power Q_s of BESS and voltage $V_{an,peak}$. (c) Responses of active and reactive powers P_P, Q_P of PV-DSTATCOM.

reactive power Q_s of the BESS and the phase voltage $V_{an,peak}$ as shown in Fig. 12(b) according to the $Q-V$ droop characteristic of the BESS. On account of the fluctuated reactive power Q_s and the phase voltage $V_{an,peak}$ at 1.5 and 3.5 s, the settling time of the active power P_s of the BESS is 761 and 752 ms, respectively. The maximum reactive power Q_s error and phase voltage $V_{an,peak}$ error are 126 Var and 18 V. Furthermore, the experimental results using the PIDNN-based PV-DSTATCOM at case 2 are represented in Fig. 13. According to the experimental result shown in Fig. 13(b) and (c), the fluctuations in the reactive power Q_s of the BESS and the phase voltage $V_{an,peak}$ are improved. Then, the settling time of the active power P_s of the BESS is reduced to be 692 and 674 ms, respectively, as shown in Fig. 13(a). The maximum reactive power Q_s error and the phase voltage $V_{an,peak}$ error are reduced to be 106 Var and 14 V. In addition, the experimental results using the FNN-based PV-DSTATCOM at case 2 are provided in Fig. 14. From the experimental results shown in Fig. 14(b) and (c), since the response of the reactive power compensation of the FNN-based PV-DSTATCOM is improved, the fluctuations in the reactive power Q_s of the BESS and the phase voltage $V_{an,peak}$ are also improved. Then, the settling time of the active power P_s of the BESS is reduced to be 632 and 621 ms, respectively, as shown in Fig. 14(a). The maximum reactive power Q_s error and the phase voltage $V_{an,peak}$ error are reduced to be 81 Var and 12 V. Additionally, the experimental results using the proposed PLFNN-based PV-DSTATCOM at case 2 are illustrated in Fig. 15. In accordance with the experimental result, because the response of the reactive power compensation of the PLFNN-based PV-DSTATCOM is much improved due to the merits of the proposed PLFNN controller, the fluctuations in the reactive power Q_s of the BESS and the phase voltage $V_{an,peak}$ are also much improved. The settling time of the active power P_s of the BESS is much reduced to be 457 ms and 451 ms, respectively. The maximum reactive

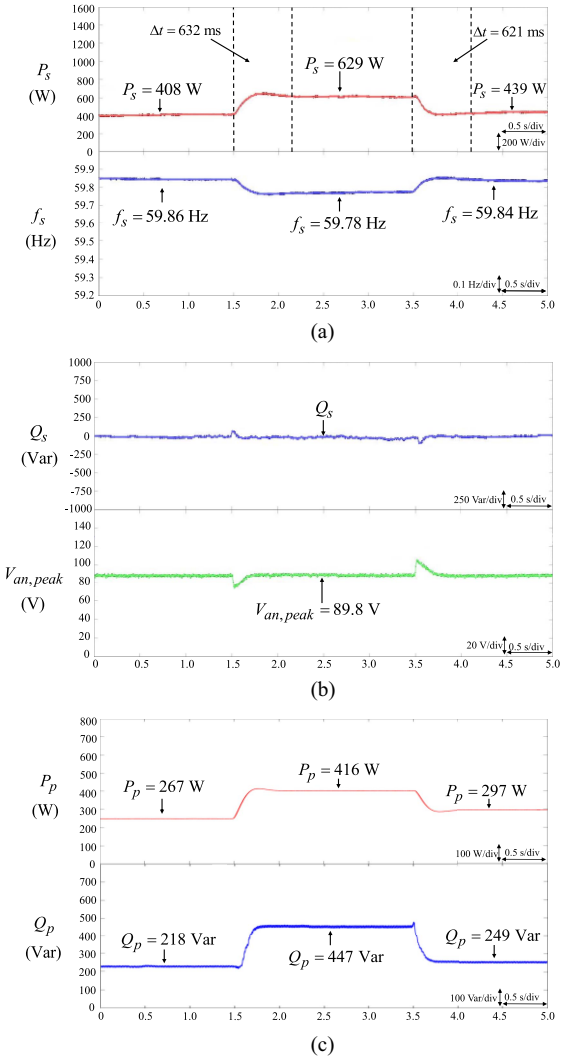

Fig. 14. Experimental results using FNN-based PV-DSTATCOM at case 2. (a) Responses of active power P_s of BESS and frequency f_s of microgrid. (b) Responses of reactive power Q_s of BESS and voltage $V_{an,peak}$. (c) Responses of active and reactive powers P_P, Q_P of PV-DSTATCOM.

TABLE III
ACTIVE POWER SETTLING TIME, MAXIMUM REACTIVE POWER Q_s ERROR AND MAXIMUM PHASE VOLTAGE $V_{an,peak}$ ERROR OF PV-DSTATCOM USING PI, PIDNN, FNN, AND PLFNN CONTROLLERS AT CASE 2

Case Conditions	Controllers	Active Power Settling Time (Load Change: 0 s →1.5 s →3.5 s)		Maximum Reactive Power Q_s Error	Maximum Voltage $V_{an,peak}$ Error
Case 2	None	523 ms	447 ms	175 Var	19 V
	PI	761 ms	752 ms	126 Var	18 V
	PIDNN	692 ms	674 ms	106 Var	14 V
	FNN	632 ms	621 ms	81 Var	12 V
	PLFNN	457 ms	451 ms	45 Var	9 V

power Q_s error and the phase voltage $V_{an,peak}$ error are also much reduced to be 45 Var and 9 V. The active power settling time, maximum reactive power Q_s error and maximum phase voltage $V_{an,peak}$ error of the PV-DSTATCOM using the PI, PIDNN, FNN and the proposed PLFNN controllers at case 2 are given in Table III. In accordance with the experimental results shown in Figs. 11–15 and Table III, owing to the merits of

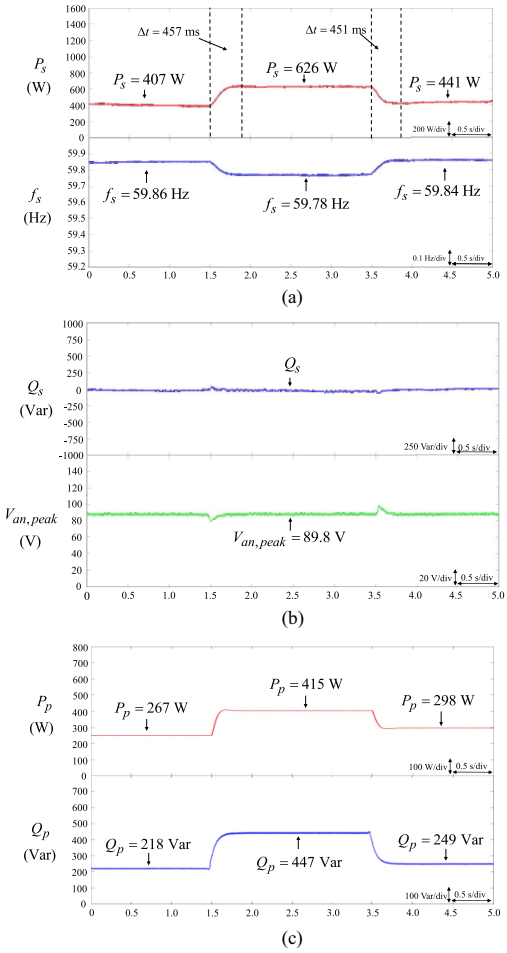

Fig. 15. Experimental results using PLFNN-based PV-DSTATCOM at case 2. (a) Responses of active power P_s of BESS and frequency f_s of microgrid. (b) Responses of reactive power Q_s of BESS and voltage $V_{an,peak}$ of microgrid. (c) Responses of active and reactive powers P_P, Q_P of PV-DSTATCOM.

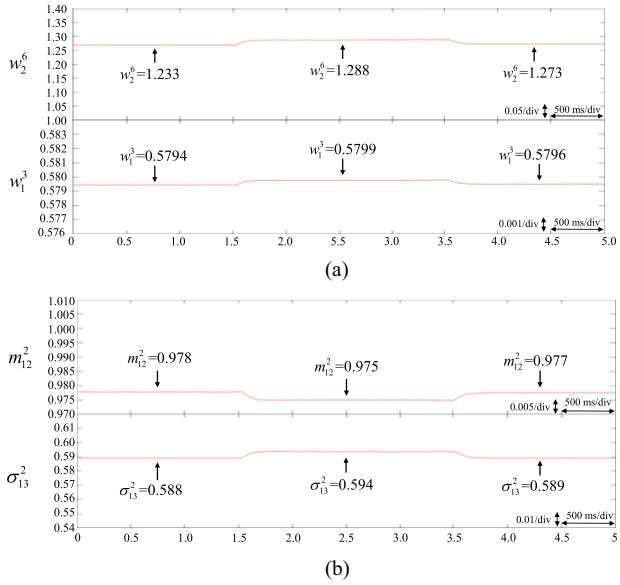

Fig. 16. Responses of network parameters of PLFNN at case 2. (a) Responses of w_2^6 and w_1^3. (b) Responses of m_{12}^2 and σ_{13}^2.

the proposed PLFNN controller to approximate, online learn, and cope with the uncertain information, the response of the reactive power compensation can be much improved by the PLFNN-based PV-DSTATCOM compared with the PI, PIDNN and FNN controllers. Hence, the settling time of the active power P_s, the fluctuations in the reactive power Q_s of the BESS and the phase voltage $V_{an,peak}$ are much improved due to the powerful robust ability of the proposed PLFNN controller.

To verify the operating performance of the online training of the network parameters of the PLFNN, the waveforms of w_2^6, w_1^3, m_{12}^2, and σ_{13}^2 of the proposed PLFNN at case 2 corresponding to the experimental results shown in Fig. 15 are provided in Fig. 16(a) and (b). According to the online learning algorithm, the parameters w_r^6, w_l^3, m_{im}^2, and σ_{im}^2 of the proposed PLFNN controller are trained online to achieve better control performance under sudden load variation. Though the network structure of the proposed PLFNN controller shown in Fig. 4 is complicated comparing with the conventional PI controller, the arithmetic capability of the adopted central processing unit in the PC is capable of implementing the control algorithms with 0.5 ms sampling time for the proposed PLFNN.

V. Conclusion

To solve the power quality issues, including the unbalanced currents, current harmonics, and lagging PF in the droop controlled microgrid, a novel control scheme of the PV-DSTATCOM has been successfully developed in this article. The developed PV-DSTATCOM owns the $\omega-P$ droop characteristic and the abilities for the power quality improvement and voltage support. Moreover, since the poor control property of the conventional PI controller results in sluggish control responses, a novel PLFNN controller was proposed to replace the PI controller for solving the disadvantages. Furthermore, in accordance with the experimental results, the current THD, PF, and CUR of the proposed PLFNN-based PV-DSTATCOM are much improved to be 2.84%, 0.99%, and 1.04%, which are superior to the PI controller with 4.48%, 0.99%, and 2.21%, PIDNN controller with 4.39%, 0.99%, and 2.13% and the FNN controller with 4.23%, 0.99%, and 1.91% owing to the powerful robust control ability of the proposed PLFNN controller. In addition, fast reactive power compensation of the proposed PLFNN-based PV-DSTATCOM can be achieved during the load changes. Therefore, the effectiveness of the proposed PLFNN-based PV-DSTATCOM for the power quality improvement and the voltage support can be ensured.

The major contributions of this article are given as follows:

1) Successful development of a novel control scheme for PV-DSTATCOM.
2) Successful development of an intelligent PLFNN controller.
3) Successful integration of the proposed PLFNN controller into the PV-DSTATCOM to effectively improve the power quality and the voltage support in a droop controlled microgrid.

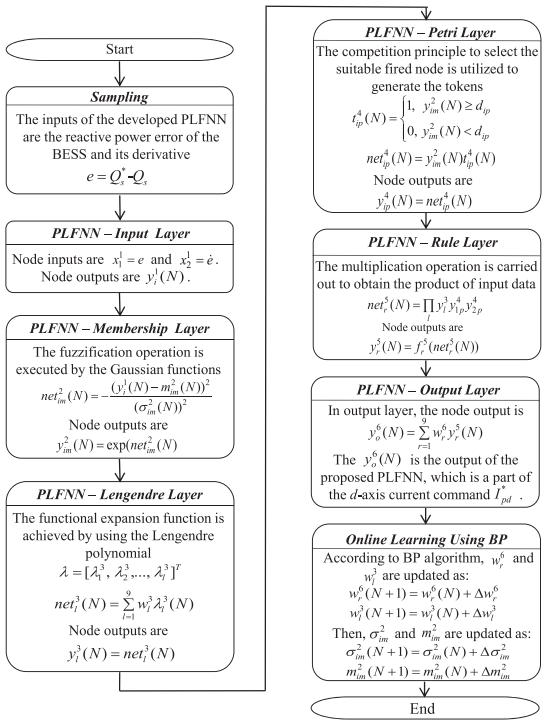

Fig. 17. Flowchart of PV-DSTATCOM using proposed PLFNN controller for reactive power compensation.

Appendix

The flowchart of PV-DSTATCOM using the proposed PLFNN controller for reactive power compensation is given in Fig. 17 and described as follows.

1) *Sampling*: In order to effectively compensate the reactive power of the droop controlled microgrid, the reactive power of the BESS is computed. Then, the reactive power error $e = Q_s^* - Q_s$ of the BESS and its derivative are obtained and sent to the proposed PLFNN controller of the PV-DSTATCOM.
2) *Input Layer*: The inputs of this layer are $x_1^1(N) = e$ and its derivative $x_2^1(N) = \dot{e}$. The node outputs $y_i^1(N)$ are transmitted to the membership layer.
3) *Membership Layer*: The Gaussian functions are adopted in this layer to implement the fuzzification operation, and the outputs $y_{im}^2(N)$ are sent to the Legendre layer.
4) *Legendre Layer*: In this layer, the Legendre polynomials are utilized as the functional expansion functions to expand the original input vector. The outputs $y_l^3(N)$ are transmitted to the Petri layer.
5) *Petri Layer*: The suitable fired node is utilized in Petri layer for generating the tokens and the transition becomes enabled state. The node outputs $y_{ip}^4(N)$ are acquired and sent to the rule layer.
6) *Rule Layer*: The output of each node symbolized by $\prod$ in this layer is obtained by multiplying the input signals and producing the result of the multiplication. The outputs $y_r^5(N)$ are transmitted to the output layer.
7) *Output Layer*: The process of the defuzzification operation is performed in output layer via the summation operation.

Moreover, the output $y_o^6(N)$ of the proposed PLFNN controller is a part of the d-axis current command I_{pd}^* of the PV-DSTATCOM as shown in Fig. 3(a) to rapidly compensate the reactive power and enhance the power quality for the droop controlled microgrid.

8) *Online Learning Using BP*: The online parameters learning is achieved by online tuning of the connected weights w_r^6 between the output layer and the rule layer, the connected weights w_l^3 in Legendre layer, and the standard deviation σ_{im}^2 and mean m_{im}^2 of the membership functions in the membership layer using the BP algorithm.

REFERENCES

[1] J. Lu, M. Zhao, S. Golestan, T. Dragicevic, X. Pan, and J. M. Guerrero, "Distributed event-triggered control for reactive, unbalanced, and harmonic power sharing in islanded AC microgrids," *IEEE Trans. Ind. Electron.*, vol. 69, no. 2, pp. 1540–1560, Feb. 2022.

[2] F. J. Lin, K. H. Tan, C. F. Chang, M. Y. Li, and T. Y. Tseng, "Development of intelligent controlled microgrid for power sharing and load shedding," *IEEE Trans. Power. Electron.*, vol. 37, no. 7, pp. 79285–77940, Jul. 2022.

[3] K. H. Tan and T. Y. Tseng, "Seamless switching and grid reconnection of microgrid using Petri recurrent wavelet fuzzy neural network," *IEEE Trans. Power. Electron.*, vol. 36, no. 10, pp. 11847–11861, Oct. 2021.

[4] Y. Tang, Z. Tian, X. Zha, X. Li, M. Huang, and J. Sun, "An improved equal area criterion for transient stability analysis of converter-based microgrid considering nonlinear damping effect," *IEEE Trans. Power. Electron.*, vol. 37, no. 9, pp. 11272–112284, Sep. 2022.

[5] P. P. Vergara, J. C. López, M. J. Rider, and L. C. P. da Silva, "Optimal operation of unbalanced three-phase islanded droop-based microgrids," *IEEE Trans. Smart Grid*, vol. 10, no. 1, pp. 928–940, Jan. 2019.

[6] J. F. Patarroyo-Montenegro, F. Andrade, J. M. Guerrero, and J. C. Vasquez, "A linear quadratic regulator with optimal reference tracking for three-phase inverter-based islanded microgrids," *IEEE Trans. Power. Electron.*, vol. 36, no. 6, pp. 7112–7122, Jun. 2021.

[7] G. Agundis-Tinajero et al., "Extended-optimal-power-flow-based hierarchical control for islanded AC microgrids," *IEEE Trans. Power. Electron.*, vol. 34, no. 1, pp. 840–848, Jan. 2019.

[8] W. Yuan, Y. Wang, and Z. Chen, "New perspectives on power control of AC microgrid considering operation cost and efficiency," *IEEE Trans. Power Syst.*, vol. 36, no. 5, pp. 4844–4847, Sep. 2021.

[9] Z. Li, Z. Cheng, J. Liang, J. Si, L. Dong, and S. Li, "Distributed event-triggered secondary control for economic dispatch and frequency restoration control of droop-controlled AC microgrids," *IEEE Trans. Sustain. Energy*, vol. 11, no. 3, pp. 1938–1950, Jul. 2020.

[10] K. H. Tan, M. Y. Li, and X. Y. Weng, "Droop controlled microgrid with DSTATCOM for reactive power compensation and power quality improvement," *IEEE Access*, vol. 10, pp. 121602–121614, 2022.

[11] P. A. Afsher, M. V. Manoj Kumar, C. M. Nirmal Mukundan, and K. Shyju, "A PV-DSTATCOM with adaptive DC-link voltage for grid integration and PQ enhancement," *IEEE Trans. Ind. Appl.*, vol. 58, no. 5, pp. 6471–6484, Oct. 2022.

[12] Z. Bai et al., "A capacitive-coupling winding tap injection DSTATCOM integrated with distribution transformer for balance and unbalance operations," *IEEE Trans. Ind. Electron.*, vol. 70, no. 2, pp. 1081–1093, Feb. 2023.

[13] K. K. Prasad, H. Myneni, and G. S. Kumar, "Power quality improvement and PV power injection by DSTATCOM with variable DC link voltage control from RSC-MLC," *IEEE Trans. Sustain. Energy*, vol. 10, no. 2, pp. 876–885, Apr. 2019.

[14] M. Badoni, A. Singh, and B. Singh, "Power quality enhancement using Euclidean direction search based control technique," *IEEE Trans. Ind. Electron.*, vol. 67, no. 3, pp. 2231–2240, Mar. 2020.

[15] C. Balasundar, C. K. Sundarabalan, S. N. Santhanam, J. Sharma, and J. M. Guerrero, "Mixed step size normalized least mean fourth algorithm of DSTATCOM integrated electric vehicle charging station," *IEEE Trans. Ind. Inform.*, vol. 19, no. 6, pp. 7583–7591, Jun. 2023.

[16] J. Ye, H. B. Gooi, X. Zhang, and H. H. C. Iu, "Simplified four-level inverter-based single-phase DSTATCOM using model predictive control," *IEEE J. Emerg. Sel. Topics Power Electron.*, vol. 8, no. 4, pp. 3382–3395, Dec. 2020.

[17] K. H. Tan, F. J. Lin, C. Y. Tsai, and Y. R. Chang, "A distribution static compensator using a CFNN-AMF controller for power quality improvement and DC-link voltage regulation," *Energies*, vol. 11, no. 8, pp. 1–17, Aug. 2018.

[18] L. S. Czarnecki, "Instantaneous reactive power p-q theory and power properties of three-phase systems," *IEEE Trans. Power Del.*, vol. 21, no. 1, pp. 362–367, Jan. 2006.

[19] W. Freitas, A. Morelato, W. Xu, and F. Sato, "Impacts of AC generators and DSTATCOM devices on the dynamic performance of distribution systems," *IEEE Trans. Power Del.*, vol. 20, no. 2, pp. 1493–1501, Apr. 2005.

[20] X. Zhou, W. Zhong, Y. Ma, K. Guo, J. Yin, and C. Wei, "Control strategy research of D-STATCOM using active disturbance rejection control based on total disturbance error compensation," *IEEE Access*, vol. 9, pp. 50138–50150, 2021.

[21] R. J. Wai, M. W. Chen, and Y. K. Liu, "Design of adaptive control and fuzzy neural network control for single-stage boost inverter," *IEEE Trans. Ind. Electron.*, vol. 62, no. 9, pp. 5434–5445, Sep. 2015.

[22] M. K. Behera and L. C. Saikia, "A seamless control of grid-connected PV system for alleviating PV penetration in rural grid using supercapacitor accompanying with DSTATCOM and improved CTF control," *IEEE Trans. Ind. Appl.*, vol. 60, no. 2, pp. 3588–3602, Apr. 2024.

[23] P. A. M. Devan, F. A. B. Hussin, R. Ibrahim, K. Bingi, and H. Q. A. Hbdulrab, "Fractional-order predictive PI controller for dead-time processes with set-point and noise filtering," *IEEE Access*, vol. 8, pp. 183759–183773, 2020.

[24] R. K. Jain, V. R. Barry, and H. K. V. Gadiraju, "Model-based design and sliding mode control approach for two-stage water pumping system with reduced sensor," *IEEE J. Emerg. Sel. Topics Power Electron.*, vol. 10, no. 4, pp. 3940–3949, Aug. 2022.

[25] R. J. Wai and C. C. Chu, "Motion control of linearinduction motor via Petri fuzzy neural network," *IEEE Trans. Ind. Electron.*, vol. 54, no. 1, pp. 281–295, Feb. 2007.

[26] F. J. Lin, P. L. Wang, and I. M. Hsu, "Intelligent nonsingular terminal sliding mode controlled nonlinear time-varying system using RPPFNN-AMF," *IEEE Trans. Fuzzy Syst.*, vol. 32, no. 3, pp. 1036–1049, Mar. 2024.

[27] B. Huang and M. Zhou, "Symbolic scheduling of robotic cellular manufacturing systems with timed Petri nets," *IEEE Trans. Control Syst. Technol.*, vol. 30, no. 5, pp. 1876–1887, Sep. 2022.

[28] F. J. Lin, C. I. Chen, G. D. Xiao, and P. R. Chen, "Voltage stabilization control for microgrid with asymmetric membership function-based wavelet Petri fuzzy neural network," *IEEE Trans. Smart Grid*, vol. 12, no. 5, pp. 3731–3741, Sep. 2021.

[29] K. H. Tan, "Squirrel cage induction generator system using wavelet Petri fuzzy neural network control for wind power applications," *IEEE Trans. Power Electron.*, vol. 31, no. 7, pp. 5242–5254, Jul. 2016.

[30] J. Chen and L. Xu, "Improved modeling and generalization capabilities of graph neural networks with Legendre polynomials," *IEEE Access*, vol. 11, pp. 63442–63450, 2023.

[31] S. Khorashadizadeh and A. A. Kalat, "Adaptive back-stepping cancer control using Legendre polynomials," *IET Syst. Biol.*, vol. 14, no. 1, pp. 8–15, Feb. 2019.

[32] F. J. Lin, M. S. Huang, S. G. Chen, and C. W. Hsu, "Intelligent maximum torque per ampere tracking control of synchronous reluctance motor using recurrent Legendre fuzzy neural network," *IEEE Trans. Power Electron.*, vol. 34, no. 12, pp. 12080–12094, Dec. 2019.

[33] F. J. Lin, M. S. Huang, C. Y. Hung, and Y. C. Chien, "Intelligent computed torque control with recurrent Legendre fuzzy neural network for permanent-magnet assisted synchronous reluctance motor," *IEEE Access*, vol. 11, pp. 54017–54028, 2023.

[34] L. Du, M. Li, Z. Tang, L. Xiong, X. Ma, and G. Tang, "A fast positive sequence components extraction method with noise immunity in unbalanced grids," *IEEE Trans. Power Electron.*, vol. 35, no. 7, pp. 6682–6685, Jul. 2020.

[35] A. Ranjan, S. Kewat, and B. Singh, "DSOGI-PLL with in-loop filter based solar grid interfaced system for alleviating power quality problems," *IEEE Trans. Ind. Appl.*, vol. 57, no. 1, pp. 730–740, Feb. 2021.

[36] P. Rodriguez, A. V. Timbus, R. Teodorescu, M. Liserre, and F. Blaabjerg, "Flexible active power control of distributed power generation systems during grid faults," *IEEE Trans. Ind. Electron.*, vol. 54, no. 5, pp. 2583–2592, Oct. 2007.

[37] S. Y. Chen and F. J. Lin, "Decentralized PID neural network control for five degree-of-freedom active magnetic bearing," *Eng. Appl. Artif. Intell.*, vol. 26, no. 3, pp. 962–973, Mar. 2013.

Faa-Jeng Lin (Fellow, IEEE) received B.S. and M.S. degrees in electrical engineering from National Cheng Kung University, Tainan, Taiwan, and the Ph.D. degree in electrical engineering from National Tsing Hua University, Hsinchu, Taiwan, in 1983, 1985, and 1993, respectively.

He is currently a Chair Professor with the Department of Electrical Engineering, National Central University, and Deputy Minister, National Science and Technology Council, Taiwan. His work has been widely cited. Several of his papers have helped to establish research areas such as fuzzy neural network control of motor drives, motion control systems, and smart grids. His research interests include ac motor drives, power electronics, renewable energies, smart grids, intelligent and nonlinear control theories.

Dr. Lin was the Dean with the College of Electrical Engineering and Computer Science, National Central University, Taiwan; the President with Taiwan Smart Grid Industry Association; and the President with the National Applied Research Laboratories, Taiwan. He is currently an Associate Editor for IEEE TRANSACTION ON POWER ELECTRONICS and IEEE TRANSACTION ON FUZZY SYSTEMS, and the Executive Director of Taiwan Power Company. He was the recipient of the Outstanding Research Awards from the National Science Council, Taiwan, in 2004, 2010 and 2013; Outstanding Professor of Engineering Award in 2016 from the Chinese Institute of Engineers, Taiwan; 29th TECO Award, 2022, Taiwan; Outstanding Contribution Award of Power Electronics, Taiwan Power Electronics Association, 2023; Engineering Medal of Electrical Engineering, The Chinese Institution of Electrical Engineering, Taiwan, 2024. He is also an IET/CIEE/AAIA Fellow.

Kuang-Hsiung Tan (Member, IEEE) received the B.S., M.S., and Ph.D. degrees from the Chung Cheng Institute of Technology (CCIT), National Defense University, Taoyuan, Taiwan, in 2002, 2007, and 2013, respectively, all in electrical and electronic engineering.

He has been a Faculty Member with CCIT, where he is currently an Associate Professor with the Department of Electrical and Electronic Engineering. His teaching and research interests include power electronics, power quality, microgrid systems, and intelligent control.

Zhao-Yun Kuan received the B.S. degree in undergraduate program of vehicle and energy engineering from the National Taiwan Normal University, Taipei, Taiwan, in 2022. He is currently working toward the M.S. degree in intelligent PV-DSTATCOM for power quality improvement with the National Central University, Chungli, Taiwan.

His research interests include dynamic DSTATCOM, microgrid, intelligent control, and power electronics.

Chen-Yi Wang received the B.S. degree in optics and photonics in 2023 from the National Central University, Chungli, Taiwan, where she is currently working toward the M.S. degree in intelligent pry-synchronization for grid reconnection.

Her research interests include microgrid, intelligent control, and power electronics.